

# Time-Resolved Far Infrared Light Transport Decomposition for Thermal Photometric Stereo

Kenichiro Tanaka<sup>1</sup>, Member, IEEE, Nobuhiro Ikeya, Tsuyoshi Takatani, Member, IEEE, Hiroyuki Kubo<sup>2</sup>, Takuya Funatomi<sup>2</sup>, Member, IEEE, Vijay Ravi<sup>3</sup>, Member, IEEE, Achuta Kadambi, Member, IEEE, and Yasuhiro Mukaigawa<sup>3</sup>, Member, IEEE

**Abstract**—We present a novel time-resolved light transport decomposition method using thermal imaging. Because the speed of heat propagation is much slower than the speed of light propagation, the transient transport of far infrared light can be observed at a video frame rate. A key observation is that the thermal image looks similar to the visible light image in an appropriately controlled environment. This implies that conventional computer vision techniques can be straightforwardly applied to the thermal image. We show that the diffuse component in the thermal image can be separated, and therefore, the surface normals of objects can be estimated by the Lambertian photometric stereo. The effectiveness of our method is evaluated by conducting real-world experiments, and its applicability to black body, transparent, and translucent objects is shown.

**Index Terms**—Photothermal effects, photometry, transient analysis, image decomposition

## 1 INTRODUCTION

LIGHT transport is a study of the complex interaction between light and matter. Decomposing light transport powers low-level computer vision tasks that range from shape recovery to reflectance estimation. Previous work has studied light transport at visible light wavelengths; here we lay the foundation for light transport at long-wave infrared wavelengths. At these wavelengths, light transport is very unique due the interplay between heat and long-wave infrared light.

Previously, color [1], polarization [2], and active illumination [3] have been used for light transport decomposition. The transient behaviour of optical components varies in the order of tens of picoseconds [4] thus paving way for time-resolved approaches. So far, multiple time-resolved approaches have been proposed—with the use of a femto-pulsed laser, interferometer [5], time-of-flight camera modifications [6], [7], [8], and single-photon sensor [9].

Unlike visible light imaging, time-resolved light transport decomposition using thermal imaging is feasible at a video frame rate. This is because of the important observation that the speed of heat propagation is much slower than the speed of light propagation. Inspired by this, we develop a novel time-resolved decomposition technique for far infrared light transport.

Thermal imaging has been traditionally considered as being different from visible light imaging: While the thermal image is a representation of the temperature of the object, the visible light image is a description of the visual information. However, we show that when the imaging environment is appropriately controlled, similar patterns are observed in both the thermal and visible light imaging. This is because thermal imaging is a technique to observe light on far infrared wavelength. Fig. 1 shows an image captured by a color camera and a thermal image, where a ball is illuminated by a point light source. Both the color image and the thermal image exhibit the similar shading. This observation implies that computer vision techniques can also be applied for thermal images.

### Contributions

In this study, a time-resolved approach for decomposition of the far infrared light transport is proposed for a photometric stereo application. With the help of physical law of heat and thermodynamics, we show that far infrared light transport can be considered as a composition of multiple optical and thermal effects similar to the visible light transport. We propose definitions of the ambient, the reflection, the diffuse radiation, and the global radiation components in the thermal framework and describe the transient properties of each. We also provide an application of our approach. We show that the surface normal can be estimated based on the Lambertian photometric stereo, because the diffuse component of the far infrared light, which follows the cosine law, is separated.

- K. Tanaka is with the Department of Information Science, Nara Institute of Science and Technology (NAIST)8916-5 Takayama, Ikoma, Nara 630-0192, Japan, and also with the University of California, Los Angeles (UCLA)420 Westwood Plaza, Los Angeles, CA 90095 USA. E-mail: ktanaka@is.naist.jp.
- N. Ikeya, H. Kubo, T. Funatomi, and Y. Mukaigawa are with the Department of Information Science, Nara Institute of Science and Technology (NAIST)8916-5 Takayama, Ikoma, Nara 630-0192, Japan. E-mail: {ikeya.nobuhiro.i16, hkubo, funatomi, mukaigawa}@is.naist.jp.
- T. Takatani is with the National Institute of Informatics2-1-2 Hitotsubashi, Chiyoda, Tokyo 101-8430, Japan. E-mail: takatani.tsuyoshi.to2@is.naist.jp.
- V. Ravi and A. Kadambi are with the University of California, Los Angeles (UCLA)420 Westwood Plaza, Los Angeles, CA 90095 USA. E-mail: vijaysumaravi@ucla.edu, achuta@ee.ucla.edu.

Manuscript received 28 May 2019; revised 4 Oct. 2019; accepted 2 Dec. 2019. Date of publication 18 Dec. 2019; date of current version 5 May 2021. (Corresponding author: Kenichiro Tanaka.) Recommended for acceptance by K. Nishino. Digital Object Identifier no. 10.1109/TPAMI.2019.2959304

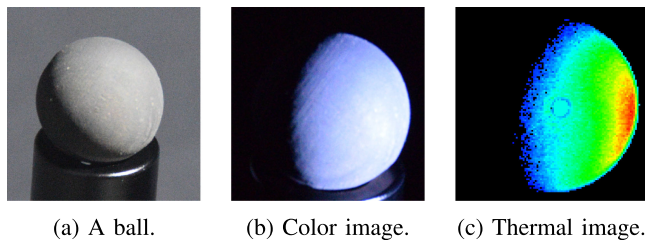


Fig. 1. A ball captured by a conventional color camera and a thermal camera. (a) The target object. (b) Reflection image using a conventional camera. (c) Thermal image of the same object. When the object is carefully illuminated, shading of both images are same, which implies conventional computer vision techniques can be applied to the thermal images.

The chief contributions of this study are threefold. First, we extend the visible light transport model to the far infrared light transport. We show that the thermal image is a composition of ambient, reflection, diffuse, and global components, which is similar to the visible light transport. Second, a novel approach for time-resolved light transport decomposition is provided based on the difference of the transient property of the far infrared light transport. Finally, we show that ordinary computer vision techniques can be straightforwardly applied to thermal images. As a proof of the concept, we propose a method to recover the surface normal using photometric stereo after decomposing the far infrared light transport. The surface normal of challenging objects that have complicated optical effects can be recovered.

The proposed thermal photometric stereo can be applied for any objects that absorb light and convert it into heat, including black body, transparent, and translucent objects. It has a wide applicability compared with the photometric stereo using visible light.

In this work, we extend our prior work [10] with the following additions:

- 1) We provide theoretical justification to the light transport decomposition using law of thermodynamics. We support our explanation with analytical proofs.
- 2) We show that the simulations and experimental observations for objects with different material properties agrees with the dual exponential model as proposed in [10].

The paper is organized as follows: in Section 2 we briefly review the literature in light transport for thermal imaging and surface normal estimation. In Section 3, we describe the components of the thermal light transport and provide physical justification and simulation to support our claims. We present the thermal light transport decomposition and surface normal estimation method in Section 4. Section 5 describes the experiments being performed in this study and Section 6 concludes this paper.

## 2 RELATED WORK

This paper lies at the intersection of thermal imaging, light transport decomposition, and photometric stereo. We summarize prior work in these three areas.

### 2.1 Light Transport Decomposition

Light transport decomposition represents a principled study of how light propagates from an illumination source to

camera sensor. This area of research is organized into sub-fields based upon the physics of capture setups.

*Color-based* approaches were among the first to be employed for light transport decomposition. The dichromatic reflectance model by Shafer *et al.* [1] proposes that specular reflection depends on the color of the light source while diffuse reflection depends on the color of the object. Several methods [11], [12], [13] use this model for the separation of the diffuse and the specular reflections.

*Polarization-based* approaches use polarizers to separate light transport. Separation of diffuse and specular reflections using linear polarization was demonstrated by Wolff and Boulton [14]. Treibitz and Schechner [2] showed separation of diffuse reflection and volumetric scattering using circular polarization.

*Active illumination* has also proved to be a successful tool to decompose light transport. Nayar *et al.* [3] used high frequency projection patterns to separate direct and global reflection components of the visible imaging light transport. There have been several extensions proposed to this—environmental illumination for separation of diffuse and specular reflections by Lamond *et al.* [15], transmission and scattering [16], and single scattering and multiple scattering [17]. O’Toole *et al.* [18], [19], [20] decompose light transport using an epipolar constraint. Although we utilize active illumination, as per our knowledge, this is the first study in light transport decomposition of thermal images in the far infrared wavelength.

*Time-resolved decomposition* is one of the latest technologies in the domain of light transport decomposition. The temporal response of a femtosecond-pulsed laser was exploited by Wu *et al.* [4] to develop a method to decompose diffuse reflection, inter-reflection, and subsurface scattering. Resolving the multi-path interference problem in the time-of-flight camera is an active research topic and has been studied by assuming the two-bounce or simplified reflection models [21], [22], [23], [24],  $K$ -sparsity [25], [26], [27], parametric model [28], [29], consistency between ToF and stereo [30], simplified indirect reflections [31], and large-scale multi-path [32]. It can be used to measure a slice of BRDF [33], perform non-line-of-sight imaging [34], [35], [36], and recover the shape of transparent and translucent objects [37], [38]. Past work using time resolved methods [4], [5], [39], [40] also separate direct and indirect light transports.

*Far Infrared Heating Characteristics* are known to have the temporal transience. Thompson *et al.* [41] model the temporal effects of heating during infrared neural stimulation. Ito *et al.* [42] describe the heating effects in skin during continuous wave near infrared spectroscopy. We define far infrared light transport components as light and heat, from the law of thermodynamics and simulation.

### 2.2 Computational Thermal Imaging

Thermal imaging approaches, have traditionally, not been widely used to solve computer vision problems. Saponaro *et al.* [43] estimate the material from the water permeation and heating/cooling process of the object. Miyazaki *et al.* [44] resolve the ambiguity regarding polarization-based shape reconstruction using a thermal image. Eren *et al.* [45] recover the transparent shape by triangulation using laser beam spot

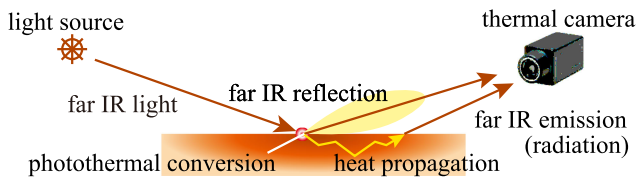


Fig. 2. Far infrared light transport. While far infrared light can partially be reflected on the surface, the rest of the light is converted to heat energy, propagates inside the object, and is then converted to far infrared light corresponding to the temperature. The composition of all the components are captured by a camera. The observation system is closed in the far infrared light domain.

heating and thermal imaging. In this paper, we first propose a light transport model of thermal imaging.

### 2.3 Photometric Stereo

Photometric stereo has been a broad interest in the computer vision field. The Lambertian photometric stereo [46] is a standard way to recover the surface normal by assuming Lambert reflection, no optical effect such as shadow and scattering, orthogonal projection, and parallel lights. To apply the Lambertian photometric stereo for a non-Lambert surface, other optical components need to be separated by pattern projection [3], polarization [47], and fluorescence [48]. Similar to these approaches, we apply the Lambertian photometric stereo after extracting the diffuse component.

Inoshita *et al.* [49] improves the photometric stereo for translucent objects using surface normal deconvolution, Ngo *et al.* [50] use a polarization cue to recover a smooth surface, and Murez *et al.* [51] develop photometric stereo in a scattering media that consider the blur depending on the distance. While these methods jointly compensate for the global light transport in their solutions, we aim to separate the far infrared light transport.

## 3 FAR INFRARED LIGHT TRANSPORT

We begin by establishing a few basic principles pertaining to thermal and far infrared light transport. In particular, we will establish a theory of light transport for *thermal cameras*.

A thermal camera is a unique camera that is designed to measure the intensity of far infrared light ( $8 - 14 \mu\text{M}$ ). A typical sensor as shown in Fig. 4, measures the intensity of far infrared light, which corresponds to the temperature. When the object is a black body, the temperature and the intensity of far infrared light are governed by the Stefan-Boltzmann law [52], which represents a one-to-one correspondence between temperature and intensity

$$E = \sigma T^4, \quad (1)$$

where  $E$  is the intensity of the radiated far infrared light,  $\sigma$  is the Stefan-Boltzmann constant,<sup>1</sup> and  $T$  is the thermodynamic temperature.

Considering the scene is illuminated by a stable parallel light source of far infrared light and the object is captured by a thermal camera as shown in Fig. 2. When the object is not a black body, a part of the far infrared light reflects on the surface, while the rest of the light is absorbed and

converted to the heat energy, the temperature increases, and far infrared light is emitted corresponding to its temperature. The observation is the sum of these effects and we term this total energy transport as *far infrared light transport*.

Although analogous light transport effects can be observed between ordinary and thermal cameras, the underlying causes can be fundamentally distinct. An image captured by an ordinary camera is the composition of multiple light transport effects, e.g., specular and diffuse reflections, inter-reflection, and subsurface scattering. Analogously, the thermal image is a sum of the multiple far infrared light transports as shown in Fig. 3. The key difference lies in the optical factors behind these light transport effects.

Here, we consider one such optical factor: the transience of light transport for a planar object. Transient light transport is observable at video frame rates for thermal cameras. This is due to the slow propagation of heat. In contrast, the transient state of ordinary light transport is dependent on the speed of light rather than of heat propagation. Fig. 5 illustrates a concept of the temperature transition of the far infrared light transport components. Before the light source is turned on, the observation consists of only the ambient component. The reflection appears immediately after the light source is turned on, and diffuse and global radiation slowly appear as the temperature increases. Then, the diffuse radiation reaches the steady state faster than the global radiation.

The observed thermal image  $I(t)$  at a video frame  $t$  can be modeled as

$$I(t) = A(t) + S(t) + D(t) + G(t), \quad (2)$$

where  $A, S, D, G$  are the ambient, reflection, diffuse radiation, and global radiation components, respectively. The time parameter  $t$  is referenced such that  $t = 0$  refers to the time that the light is turned on. In what follows, we define the 4 components and provide supporting physical justifications.

**Definition 1.** The original temperature  $T_{obj}$  of the object is defined as the temperature when the light source is turned off, i.e.,  $t < 0$ . The ambient component  $A(t)$  is the radiation emitted by the object due to the original temperature  $T_{obj}$  of the object as shown in Fig. 3a.

**Claim 1.** The ambient component,  $A(t)$ , is a time-invariant function.

**Proof.** The Stefan-Boltzmann Law (Equation (1)) can be rewritten in terms of the ambient component, such that

$$A(t) = \epsilon \sigma T_{obj}^4, \quad (3)$$

where  $\epsilon$  is the emissivity of the non black-body object. Because no heat source or sink are present when the light source is turned off,  $T_{obj}$  is constant. Then, since  $T_{obj}$  is constant, it follows from Equation (3) that  $A(t)$  is time-invariant.  $\square$

**Definition 2.** The reflection component  $S(t)$  is the far infrared light reflected off of the object when irradiated by an external source as shown in Fig. 3b.

**Claim 2.** The reflection component  $S(t)$  is a time-invariant function of the thermal reflectance.

1. Stefan-Boltzmann constant:  $\sigma = 5.67 \times 10^{-8} \text{W m}^{-2} \text{K}^{-4}$

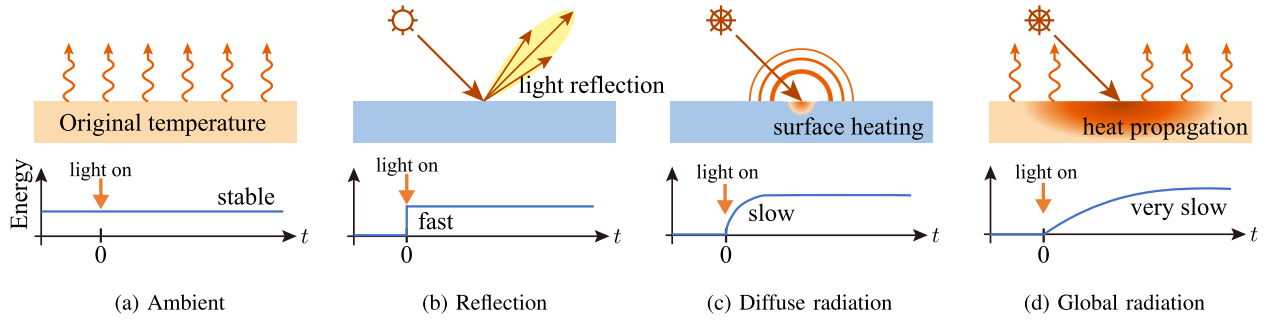


Fig. 3. Far infrared light and heat transport components. Similar to the visible light transport, far infrared light transport consists of (a) ambient, which is the original temperature, (b) reflection as light, (c) diffuse radiation, and (d) global radiation caused by heat propagation. Because the speed of heat is slower than that of light, every components has distinctive transient properties; hence, they are separable.

**Proof.**  $S(t)$  refers to the reflective component of long-wave infrared (LWIR) light radiation. Similar to visible light, the LWIR bidirectional reflectance distribution function (BRDF) is assumed to be time-invariant. As shown in Fig. 3, the incident light is directional along  $S(t)$  to be written as a single integral over the reflectance angles

$$S(t) = L_0 \int_{2\pi} R_i(\Omega) d\Omega, \quad (4)$$

where  $d\Omega$  is the differential solid angle over which reflectance varies,  $R_i(\cdot)$  is the reflectance function, and  $L_0$  is the incident light. Since neither  $L_0$  nor  $R_i(\cdot)$  vary with time,  $S(t)$  is time-invariant.  $\square$

**Corollary 1.** The previous proof assumes that the reflectance function is time-invariant. This is a standard assumption, though there are edge cases where the reflectance may vary with time [53]. These edge cases are not unique to thermal light transport, and are therefore not a special consideration for this paper.

With the preceding two claims, we have established that neither the ambient nor reflective components exhibit transience. In what follows, we define two additional components of thermal light transport, which do exhibit transience.

**Definition 3.** The diffuse radiation component  $D(t)$  is the radiation emitted as a result of local surface heating occurring at the point of irradiance as shown in Fig. 3c.

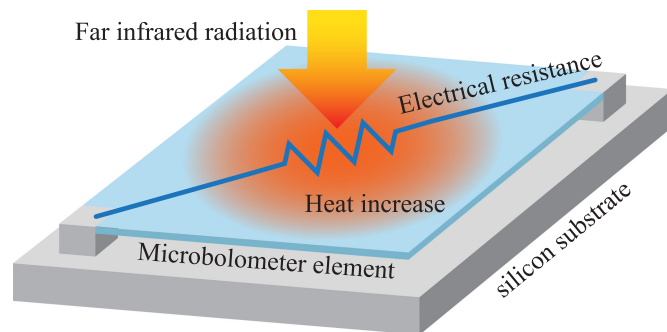


Fig. 4. The architecture of a typical thermal sensor, micro bolometer. Microbolometer element converts far infrared radiation to heat, which changes electrical resistance. The intensity of far infrared is captured by measuring the electrical resistance of the element. To prevent the surrounding temperature change, the sensor is covered by vacuum package.

**Definition 4.** The global radiation component  $G(t)$  is the radiation emitted as a result of global heat transfer as shown in Fig. 3d.

Similar to visible light [3], we assume that the radiation due to heating is the sum of diffuse and global components. In case of visible light, it has been reported that the diffuse reflection and subsurface scattering are the same physical phenomenon [54], [55], [56]; the light scatters on or beneath the surface and eventually bounces off of the material in random directions. Diffuse reflection represents the total intensity of light close to the incident point on the surface, and the subsurface scattering represents the light at a distance away from the incident point on the surface. Although there is an intermediate state between diffuse reflection and subsurface scattering [17], modeling using two components, i.e., diffuse reflection and subsurface scattering, is consistent with prior work in light transport [3]. Inspired by previous two-component simplifications, we define two analogous components for thermal radiation. According to Definitions 3 and 4, the difference between diffuse component  $D(t)$  and global component  $G(t)$  is whether heating is local or global; diffuse radiation is the heat energy whose heating point is local and global radiation is the heat that is propagated to the other points.

**Claim 3.** The diffuse radiation component exhibits a transience and increases with time.

*Justification.* From Definition 3, the diffuse radiation component is due to the local surface heating. The phenomenon of local surface heating occurs as follows. When an object is irradiated with far infrared light, a part of energy is absorbed [52], which raises the temperature of the object. In accordance with Stefan-Boltzmann Law (Eq. (1)), this increase in temperatures results in emission of radiation. However, temperature increase is a function of time [52], and therefore the emitted radiation varies with time.  $\square$

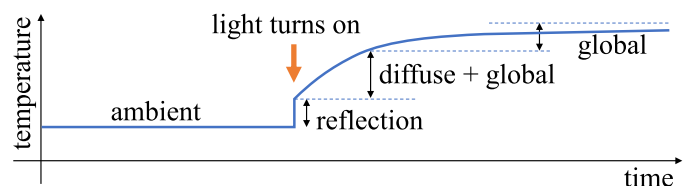


Fig. 5. Transient properties of far infrared light transport. Because the temporal responses of the components are significantly different, they can be separated from the thermal video frames.

**Claim 4.** The global radiation component exhibits a transience and increases with time.

*Justification.* From Definition 4, the global radiation component is due to the global heat transfer. The phenomenon of global heat transfer occurs as follows. When an object is irradiated for a prolonged duration of time, the absorbed energy is transferred across the spatial profile of the object, resulting in a temperature increase away from the point of irradiance (cf. [57]). The temperature gradually increases until it reaches an equilibrium state [52]. In accordance with Stefan-Boltzmann Law (Eq. (1)), the emitted radiation has an increasing transience according to the globally increasing temperature.  $\square$

**Claim 5.** The rate of increase for global radiation is slower than that of diffuse radiation.

*Justification.* From Definitions 3 and 4, the difference between global and diffuse radiations is only in the transfer of heat energy. Hence, the rate of increase in global radiation is slower than direct radiation due to the additional time taken for the heat transfer to occur across a larger spatial region.  $\square$

**Corollary 2.** The exact functions of these transiences are not obvious. Prior work in heat transfer literature [57], [58] suggests the equation takes the form of an exponential. Keeping the same functional form (i.e., an exponential) we simplify the model to include constants, such that,

$$\begin{cases} D(t) &= R_{\infty}(1 - e^{-\sigma_d t})d_{\infty} \\ G(t) &= R_{\infty}(1 - e^{-\sigma_g t})g_{\infty}, \end{cases} \quad (5)$$

where  $\sigma_d$  and  $\sigma_g$  ( $\sigma_g \ll \sigma_d$ ) represent the coefficients of the transient speed of diffuse and global radiations, respectively,  $d_{\infty}$  and  $g_{\infty}$  represent the ratios of diffuse and the global radiation components at the steady state to the total radiation, respectively, and  $R_{\infty}$  is the steady state of the radiation components.

*Validation.* To validate our model, we render the radiation transience by physical simulation and confirm our model fits the ground-truth.

Heat transfer is described using differential heat equations [58] for a hypothetical 1D object. Let  $T(x, t)$  be the temperature function where  $x$  is the variable in space and  $t$  is the variable in time. The heat equation is then

$$\frac{\partial T}{\partial t} - k \left( \frac{\partial^2 T}{\partial x^2} \right) = 0, \quad (6)$$

where,  $k$  is the thermal diffusivity. From literature [57], this equation is theoretically generalizable for a 3D object as well. This formula has the exact solution for a certain initial and boundary conditions, where the input heat is spatio-temporally impulse and the surface is infinite plane. In our case, the object is illuminated over time and area. Unfortunately, there is no closed form solution for the general case, especially for curved surfaces. Instead, we render the radiation transience and confirm how Eq. (5) approximates the ground-truth heat transfer.

Transience of the radiation can be simulated by solving the heat equation numerically. We do this by applying Forward Time Central Space (FTCS) method [59], [60] to solve

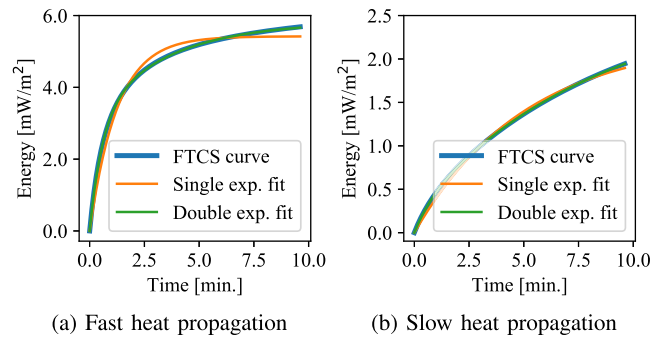


Fig. 6. Double exponential fitting result to the FTCS curves of different parameters. Double exponential is the sum of two exponentials as shown in Equation (5) representing both the direct and global components. Our model is a good approximation of the radiation transience.

Equation (6). We can estimate the change in temperature as a function of space and time for any thermal diffusivity objects. Using this simulation, we can obtain the ground-truth temperature curve, which can be used for validating our model.

To confirm that our model approximates the radiation transience, we fit the proposed double exponential model as shown in Eq. (5), which is the sum of direct and global components, to the simulated temperature curve by FTCS as shown in Fig. 6. Our model fit the FTCS curves of different thermal diffusivity 99.89 percent on average, which shows the validity of our proposed model.

## 4 DECOMPOSITION AND APPLICATION

Here, we develop an inverse problem to separate the different components of transient thermal light transport. These results also motivate a first attempt at a form of *thermal photometric stereo* (TPS).

### 4.1 Far Infrared Light Transport Decomposition

In separating different light transport components, we make the following assumptions:

- The ambient component is observed before the light source is turned on.
- Transient state of increasing temperature is observed until the temperature becomes steady.

In what follows, we expand upon the methodology of separating the different components.

#### 4.1.1 Separating the Ambient Component

The ambient component is the observation before the light source is turned on, and is determined as

$$A = I(0). \quad (7)$$

The transient observation  $T_r(t)$  is the rest of the observation, given as

$$T_r(t) = I(t) - A. \quad (8)$$

#### 4.1.2 Separating Reflection and Radiation

The reflection component is the reflection of light and has no transient state; hence it can be obtained as the increase immediately after the light source is turned on. The reflection component  $S$  is obtained as

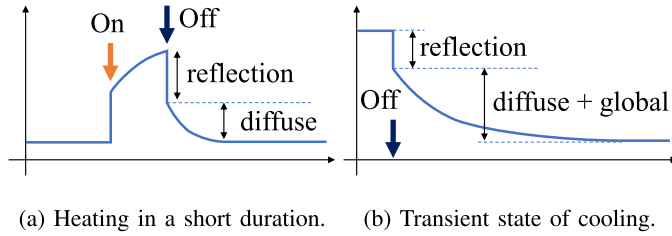


Fig. 7. Other viable approaches. (a) By turning on and off the light source in a sufficiently short time, the reflection and diffuse radiation can be directly obtained. (b) Transient state after the light source is turned off contains similar information.

$$S = T_r(\epsilon), \quad (9)$$

where  $\epsilon$  is an infinitesimal time duration.

The rest is the radiation, which has a temporal transient state. The radiation  $R(t)$  can be obtained as

$$R(t) = T_r(t) - S. \quad (10)$$

#### 4.1.3 Separating Diffuse and Global Radiation

We fit the radiation components  $R(t)$  to the model defined in Eq. (5) as

$$\begin{aligned} \hat{\sigma}_d, \hat{d}_\infty, \hat{\sigma}_g, \hat{g}_\infty &= \underset{\sigma_d, d_\infty, \sigma_g, g_\infty}{\operatorname{argmin}} \|R(t) - D(t) - G(t)\|_2^2 \\ \text{s.t. } \min_t \frac{-\log(R_\infty - R(t))}{t} &\leq \sigma_g < \sigma_d \\ 0 \leq d_\infty \leq 1 \\ 0 \leq g_\infty \leq 1 \\ d_\infty + g_\infty &= 1. \end{aligned} \quad (11)$$

The first constraint represents that the time duration to the steady state of each component is smaller than the time for the observation to reach the steady state. Because the diffuse radiation is faster than the global radiation,  $\sigma_g$  is much less than  $\sigma_d$  ( $\sigma_g \ll \sigma_d$ ). The second and third constraints represent that the intensity of the diffuse and global radiations are smaller than the total radiation. The last constraint represents that the total radiation is a sum of diffuse and global radiations, which reduces one degree of freedom. Fitting these parameters is not a convex problem so we use a grid search to find the global optimum. This does not involve a large computational cost because there are only three variables and the boundaries of the parameters can be predicted by the radiation profile  $R(t)$ .

*Other Options.* Another viable approach is to use the decrease in temperature after the light source is turned off. By switching on and off the light source over a short duration, the reflection and diffuse radiation can be directly obtained, as shown in Fig. 7a, because the effect of heat propagation is negligible over a very short time. However, the diffuse radiation does not reach the steady state, hence it may suffer from extremely low SNR. To extend the heating time could improve the SNR, however, the global radiation cannot be ignored.

The cooling process is also useful to analyze far infrared light transport as shown in Fig. 7b. Because heating and cooling are the reverse phenomena, light transport decomposition

can be achieved in a very similar way. Because this takes twice as long time, we chose to analyze only the heating process.

## 4.2 Thermal Photometric Stereo

*Thermal photometric stereo* is different from ordinary photometric stereo because it relies on the slow transience of heat propagation. The assumptions of TPS are as follows:

- Parallel far infrared light source or the light placed sufficiently far from the object is used.
- The far infrared light transport decomposition is performed for each light source direction with the same ambient temperature.

When the object is heated by a narrow beam, the point absorbs the energy and radiates far infrared light according to the increased temperature. The absorbed energy follows the cosine law [52] as is observed for the light irradiance. Since the increased temperature due to heating can be observed from any camera position, the diffuse component at the steady state can be represented as

$$D(\infty) = R_\infty d_\infty = R_\infty \rho \mathbf{i}^\top \mathbf{n}, \quad (12)$$

where  $\rho$  is the albedo of far infrared corresponding to the absorptivity, and  $\mathbf{i} \in \mathbb{R}^3$  and  $\mathbf{n} \in \mathbb{R}^3$  represent the light direction and surface normal, respectively.

Because the diffuse radiation and diffuse reflection follow the same cosine law, the ordinary photometric stereo can be applied for diffuse radiation. The ordinary photometric stereo is not applicable for black body, transparent objects, and translucent objects that does not have diffuse reflection or are governed by other light transports. However, the diffuse radiation is a phenomenon of energy absorption and emission, so the surface normal of much more objects can be uniformly obtained using diffuse radiation.

As shown in Eq. (12), the decomposed diffuse radiation follows the cosine law hence it can be directly used for the Lambertian photometric stereo. The estimated diffuse radiation component  $\hat{d}_\infty$  can be simply represented as

$$\hat{d}_\infty = \rho \mathbf{i}^\top \mathbf{n}, \quad (13)$$

where  $\rho$  is the albedo of far infrared. When multiple light sources are placed at different positions, multiple observations can be obtained that can be superposed in a matrix form as

$$\mathbf{d} = \rho \mathbf{I} \mathbf{n}, \quad (14)$$

where  $\mathbf{d}$  is the superposed diffuse components vector and  $\mathbf{I} = [\mathbf{i}_1^\top \mathbf{i}_2^\top \dots]^\top$  is the superposed light source direction matrix. When the light direction matrix is a full-rank matrix, the surface normal and albedo can be obtained as

$$\begin{cases} \mathbf{n} &= \mathbf{I}^\dagger \mathbf{d}, \\ \rho &= \|\mathbf{I}^\dagger \mathbf{d}\|_2, \end{cases} \quad (15)$$

where  $\mathbf{I}^\dagger$  is a pseudo-inverse matrix of  $\mathbf{I}$ .

## 5 EXPERIMENTS

The experimental setup is shown in Fig. 8. The target object is illuminated by far infrared spot lights (Exo Terra Heat-Glo 100W) and measured by a thermal camera (InfRec

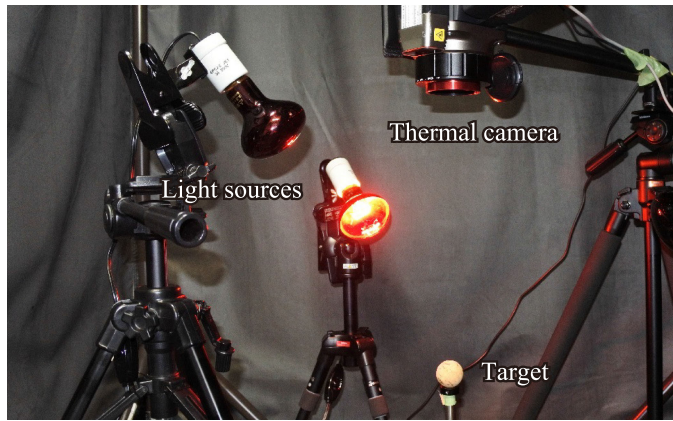


Fig. 8. Experimental setup. The object is illuminated by far infrared light and captured by a thermal camera.

R500). The ambient component is observed before the light source is turned on. Then, the light source is turned on and the change of temperature is captured as a video.

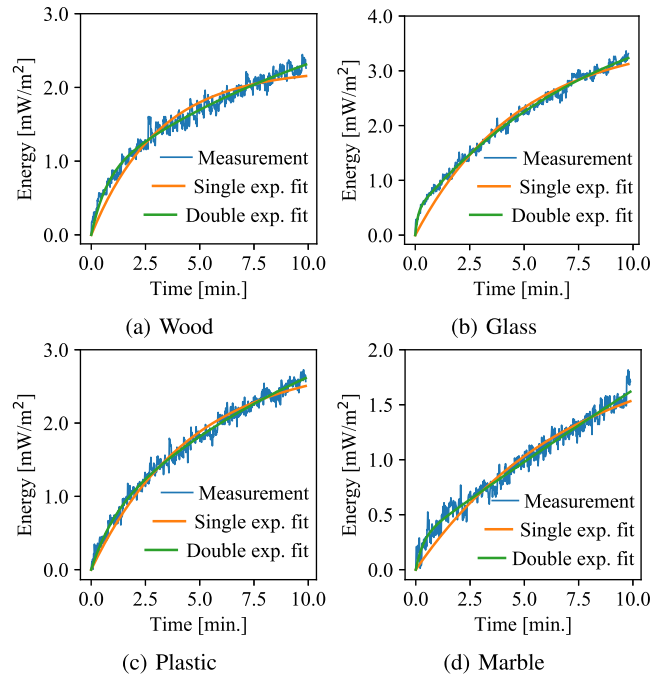


Fig. 10. Exponential fitting results. Double exponential curves fit the observation better than single exponential curves.

The real light bulb is not stable immediately after turning on and requires a warm-up period in practice. In our experiments, the bulb is warmed up outside the experiment room and brought in under a cover. Removal of the cover is the actual meaning of the light being turned on. The wall of the room is heated over the experiment time and it could become a heat source. To avoid this effect, we place the object far from the wall and the room is actively cooled using an air-conditioner.

a) *Decomposition result*: A black painted wooden sphere as shown in Fig. 9a is measured. A frame of the measured thermal video is shown in Fig. 9b. Fig. 9c shows the transition of the measured temperature at the black circular point shown in Fig. 9b. The ambient component is the measured temperature before turning on the light source, and reflection component is the increased intensity immediately after the light source is turned on. The radiation components are the rest, which is shown in Fig. 9d. The radiation components are not fitted well by a single exponential curve because this is a sum of the diffuse and global radiations. Fig. 9e shows the decomposed diffuse and global radiations. The sum of these fit well to the observation.

This procedure is applied for all the pixels, and the decomposed images are shown in Figs. 9f, 9g, and 9h. The reflection component represents the reflection of the light

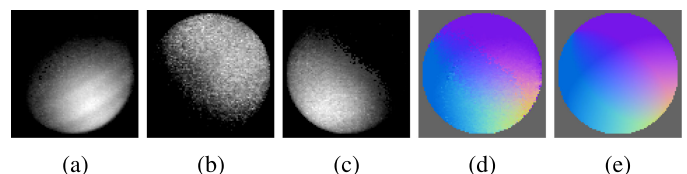
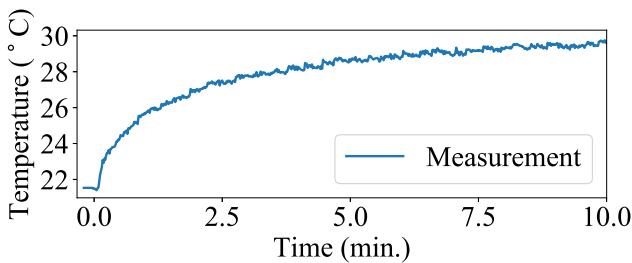
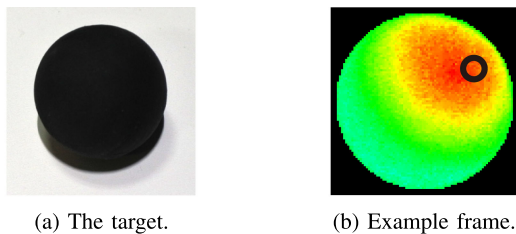
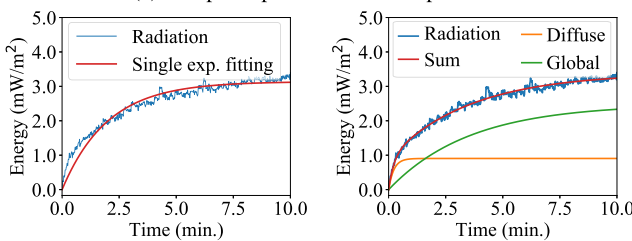


Fig. 11. Results of the thermal photometric stereo. (a-c) Decomposed diffuse radiation at different light positions. (d) Estimated surface normal. (e) The ground-truth normal.

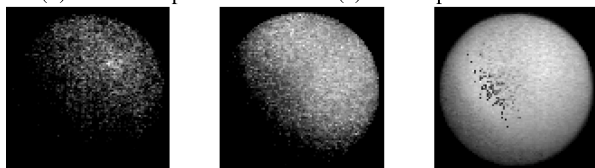


(c) Temporal profile of the temperature.



(d) Radiation profile.

(e) Decomposed radiations.



(f) Reflection comp. (g) Diffuse radiation. (h) Global radiation.

Fig. 9. Decomposition result for a black painted wooden ball. (a) The scene. (b) One of thermal video frames. Transient profiles of a point, indicated by the black circle, are shown. (c) Measured temperature transition. (d) Radiation profile. Ambient and reflection components are subtracted from (c). (e) Decomposed diffuse and global radiations. (f-h) Decomposed images of reflection, diffuse, and global radiation, respectively.

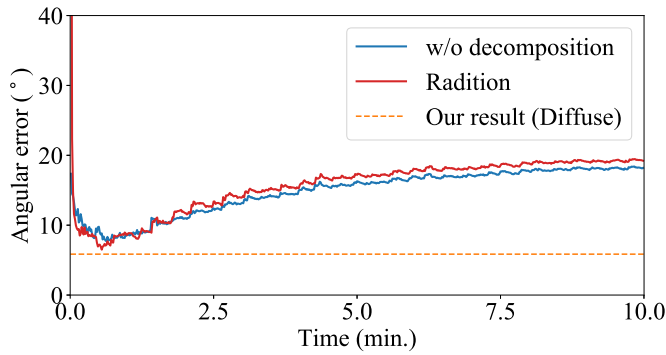


Fig. 12. The effectiveness of decomposition. Photometric stereo result without decomposition, result using radiation components, and comparison with our method. Our method is time invariant and the accuracy is shown as a dotted line. The angular error of our method is 5.85 degrees, which shows that our decomposition is effective for the separation of diffuse radiation.

source on the surface, the diffuse radiation represents the reasonable shading, and the global radiation represents the warming of the entire object.

To show that our dual exponential approximation is valid, experiments were performed on objects of four different surface properties. As shown in Fig. 10, four spherical objects made of—(a) Wood, (b) Glass, (c) Plastic and (d) Marble were chosen for this experiment, which are shown in Fig. 13. The objects were chosen so as to cover a wide range of variability in surface properties. Infrared light was irradiated and energy measurements were collected for each of the four objects. In each case, it can be observed that a dual exponential model is a better fit for the experimental measurement of energy.

*b) Surface normal estimation:* By using multiple light source positions and separating each diffuse radiation, we can apply the Lambertian photometric stereo. Fig. 11 shows the result of the thermal photometric stereo for the same object as shown in Fig. 9. A normal of the sphere is obtained as shown in Fig. 11d. The result is compared with the result without light transport decomposition (composition of reflection, diffuse, and global) and radiation (composition of diffuse and global) as shown in Fig. 12. As the temperature is not raised around  $t = 0$ , the compared results are noisy. The error increases owing to the global radiation at a longer time. As the best result, the angular errors of the result without decomposition and that of radiation is 7.71 and 6.50 degrees, respectively, while our method achieves a better result and the angular error is 5.85 degrees. This result shows the effectiveness of the separation of diffuse radiation.

We apply our method to other materials, including crystal glass, translucent plastic, and translucent marble. The decomposed diffuse component and estimated surface normal are shown in Fig. 13. Because our method is based on the diffuse radiation, materials that are difficult to measure with the ordinary vision techniques, e.g., transparent and translucent objects, can be measured in the same way. A plastic ornament is also measured, and the result shows the feasibility of our method to a complex shaped objects.

Our method is not suitable for some objects which hardly absorb the far infrared light. Metallic materials are such objects and the thermal observation of a metallic ball is shown in Fig. 14. The metallic ball reflects all the incident light and

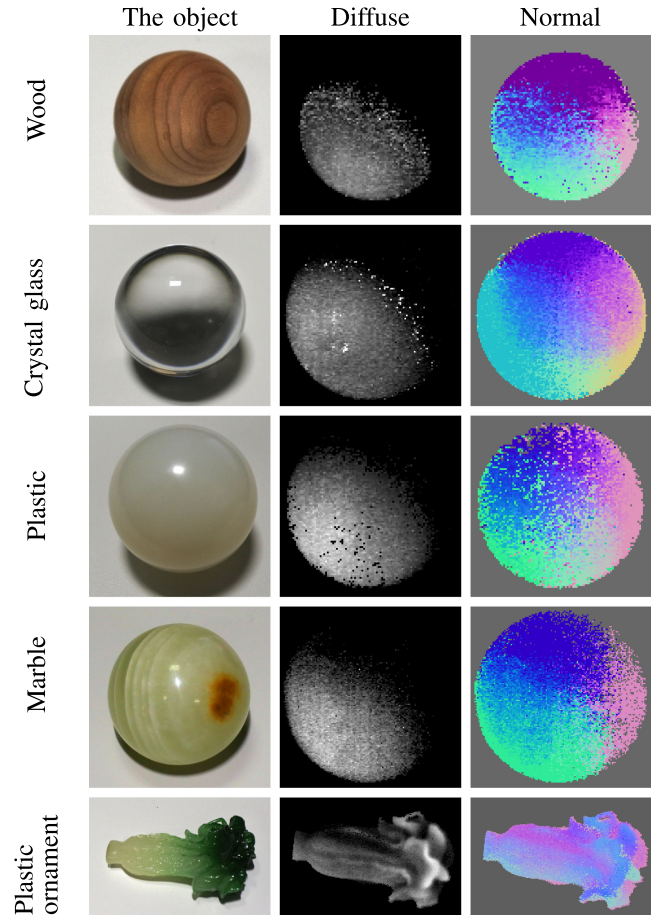


Fig. 13. Results on various materials. Spheres made by wood, crystal glass, plastic, and marble are measured, which are challenging objects for ordinary computer vision techniques. Our method uniformly recovers the surface normal for many materials. A complex shape is also measured, and our method recovers the normal appropriately.

behaves like a mirror. There is no transient state as shown in Fig. 14c which shows there are no radiation components. This problem is identical to the visible light observation.

## 6 CONCLUSION

This paper presents a novel technique for the time-resolved decomposition of far infrared light transport. We describe the far infrared light transport model, its transient properties, and that the ordinary vision techniques can be applied to decomposed thermal images. Because this is a first work

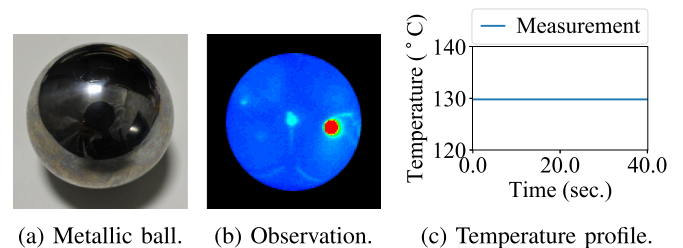


Fig. 14. A failure case. The absorption rate is too small hence the metallic ball reflects all the incident light and shows the spherical thermal map of the room. The plot shows the temporal response of the highlighted point, where no transient components are observed. In such a case, only the ambient and specular components can be obtained and the photometric stereo does not work well.

of far infrared light transport, we believe that this work will spur further researches using far infrared light transport, including thermal reflectance analysis, thermal multi-path, thermal non-line-of-sight imaging [61], material classification, and so on.

We also propose a time-resolved far infrared light transport decomposition and thermal photometric stereo as its application. Separating diffuse component of far infrared radiations, the surface normal of any objects that absorbs the incident light, including transparent, translucent, and black objects as well as matte objects are recovered.

While the effectiveness of our method is shown by some real-world experiments, some limitations are also encountered. First, the result is noisy owing to noisy observations and pixel-wise calculation. One reason is that far infrared sensors are not developed for measuring small temperature changes hence low SNR. Naturally, the quality of the sensor will be improved in the future and it will directly improve our results. A global optimization that considers smoothness or simply using a smoothing filter are other options to improve the results.

Another limitation is that some materials, such as metals, do not exhibit much diffuse radiation. In such a case, the ambient and reflection components can be separated; however, the photometric stereo is not applicable. This problem is the same as that encountered with visible light observation, e.g., photometric stereo suffers from mirror surface objects. In contrast, the absorption of many objects, including glass, is high, hence the potential applicability of our method is relatively higher than visible light observation techniques.

We only model a simple far infrared light transport. Inhomogeneous, multi-material, thin, and/or locally spiny shape has complicated heat transport thus it might not exhibit the exponential transience as in Eq. (5). Thus our method works only for locally planar, homogeneous, and sufficiently thick objects. Developing a sophisticated model for such objects is one of the interesting future directions of this research.

## ACKNOWLEDGMENTS

This work was supported in part by JSPS KAKEN grant JP18H03265, JP18K19822, JP26700013, JP15H05918, and JP17J05602. Achuta Kadambi was supported in part by an NSF Research Initiation Award (IIS 1849941).

## REFERENCES

- [1] S. A. Shafer, "Using color to separate reflection components," *Color Res. Appl.*, vol. 10, no. 4, pp. 210–218, 1985.
- [2] T. Treibitz and Y. Y. Schechner, "Active polarization descattering," *IEEE Trans. Pattern Anal. Mach. Intell.*, vol. 31, no. 3, pp. 385–399, Mar. 2009.
- [3] S. K. Nayar, G. Krishnan, M. D. Grossberg, and R. Raskar, "Fast separation of direct and global components of a scene using high frequency illumination," *ACM Trans. Graphics*, vol. 25, no. 3, pp. 935–944, 2006.
- [4] D. Wu *et al.*, "Decomposing global light transport using time of flight imaging," *Int. J. Comput. Vision*, vol. 107, no. 2, pp. 123–138, 2014.
- [5] I. Gkioulekas, A. Levin, F. Durand, and T. Zickler, "Micron-scale light transport decomposition using interferometry," *ACM Trans. Graphics*, vol. 34, no. 4, pp. 37:1–37:14, 2015.
- [6] F. Heide, M. B. Hullin, J. Gregson, and W. Heidrich, "Low-budget transient imaging using photonic mixer devices," *ACM Trans. Graphics*, vol. 32, no. 4, pp. 45:1–45:10, 2013.
- [7] A. Kadambi *et al.*, "Coded time of flight cameras: Sparse deconvolution to address multipath interference and recover time profiles," *ACM Trans. Graphics*, vol. 32, no. 6, pp. 167:1–167:10, 2013.
- [8] K. Kitano *et al.*, "Recovering temporal PSF using ToF camera with delayed light emission," *IPSJ Trans. Comput. Vision Appl.*, vol. 9, Jun. 2017, Art. no. 15.
- [9] M. O'Toole, F. Heide, D. Lindell, K. Zang, S. Diamond, and G. Wetzstein, "Reconstructing transient images from single-photon sensors," in *Proc. IEEE Conf. Comput. Vis. Pattern Recognit.*, 2017, pp. 2289–2297.
- [10] K. Tanaka, N. Ikeya, T. Takatani, H. Kubo, T. Funatomi, and Y. Mukaigawa, "Time-resolved light transport decomposition for thermal photometric stereo," in *Proc. IEEE/CVF Conf. Comput. Vis. Pattern Recognit.*, 2018, pp. 4804–4813.
- [11] Y. Sato and K. Ikeuchi, "Temporal-color space analysis of reflection," *J. Opt. Soc. America A*, vol. 11, no. 7, pp. 2990–3002, 1994.
- [12] T. Nguyen, Q. N. Vo, H.-J. Yang, S.-H. Kim, and G.-S. Lee, "Separation of specular and diffuse components using tensor voting in color images," *Appl. Opt.*, vol. 53, no. 33, pp. 7924–7936, 2014.
- [13] W. Ren, J. Tian, and Y. Tang, "Specular reflection separation with color-lines constraint," *IEEE Trans. Image Process.*, vol. 26, no. 5, pp. 2327–2337, May 2017.
- [14] L. B. Wolff and T. E. Boult, "Constraining object features using a polarization reflectance model," *IEEE Trans. Pattern Anal. Mach. Intell.*, vol. 13, no. 7, pp. 635–657, Jul. 1991.
- [15] B. Lamond, P. Peers, and P. Debevec, "Fast Image-Based Separation of Diffuse and Specular Reflections," in *Proc. SIGGRAPH Sketches*, 2007, Art. no. 74.
- [16] K. Tanaka, Y. Mukaigawa, Y. Matsushita, and Y. Yagi, "Descattering of transmissive observation using parallel high-frequency illumination," in *Proc. IEEE Int. Conf. Comput. Photography*, 2013, pp. 96–103.
- [17] Y. Mukaigawa, R. Raskar, and Y. Yagi, "Analysis of light transport in scattering media," in *Proc. IEEE Conf. Comput. Vis. Pattern Recognit.*, 2010, pp. 153–160.
- [18] M. O'Toole, R. Raskar, and K. N. Kutulakos, "Primal-dual coding to probe light transport," *ACM Trans. Graphics*, vol. 31, no. 4, pp. 39:1–39:11, 2012.
- [19] M. O'Toole, J. Mather, and K. N. Kutulakos, "3D shape and indirect appearance by structured light transport," in *Proc. IEEE Conf. Comput. Vis. Pattern Recognit.*, 2014, pp. 3246–3253.
- [20] M. O'Toole, S. Achar, S. G. Narasimhan, and K. N. Kutulakos, "Homogeneous codes for energy-efficient illumination and imaging," *ACM Trans. Graphics*, vol. 34, no. 4, pp. 35:1–35:13, 2015.
- [21] S. Fuchs, "Multipath interference compensation in time-of-flight camera images," in *Proc. IEEE Int. Conf. Pattern Recognit.*, 2010, pp. 3583–3586.
- [22] A. A. Dorrington, J. P. Godbaz, M. J. Cree, A. D. Payne, and L. V. Streeter, "Separating true range measurements from multipath and scattering interference in commercial range cameras," in *Proc. Three-Dimensional Imag. Interaction Meas.*, 2011, Art. no. 786404.
- [23] J. P. Godbaz, M. J. Cree, and A. A. Dorrington, "Closed-form inverses for the mixed pixel/multipath interference problem in AMCW lidar," in *Proc. Comput. Imag. X*, 2012, Art. no. 909778.
- [24] D. Jimenez, D. Pizarro, M. Mazo, and S. Palazuelos, "Modelling and correction of multipath interference in time of flight cameras," in *Proc. IEEE Conf. Comput. Vis. Pattern Recognit.*, 2012, pp. 893–900.
- [25] A. Bhandari, M. Feigin, S. Izadi, C. Rhemann, M. Schmidt, and R. Raskar, "Resolving multipath interference in Kinect: An inverse problem approach," in *Proc. IEEE SENSORS*, 2014, pp. 614–617.
- [26] D. Freedman, E. Krupka, Y. Smolin, I. Leichter, and M. Schmidt, "SRA: Fast removal of general multipath for ToF sensors," in *Proc. Eur. Conf. Comput. Vis.*, 2014, pp. 234–249.
- [27] H. Qiao, J. Lin, Y. Liu, M. B. Hullin, and Q. Dai, "Resolving transient time profile in ToF imaging via log-sum sparse regularization," *Opt. Letters*, vol. 40, no. 6, pp. 918–21, 2015.
- [28] F. Heide, L. Xiao, A. Kolb, M. B. Hullin, and W. Heidrich, "Imaging in scattering media using correlation image sensors and sparse convolutional coding," *Opt. Express*, vol. 22, no. 21, pp. 26 338–26 350, 2014.
- [29] A. Kirmani, A. Benedetti, and P. A. Chou, "SPUMIC: Simultaneous phase unwrapping and multipath interference cancellation in time-of-flight cameras using spectral methods," in *Proc. IEEE Int. Conf. Multimedia Expo*, 2013, pp. 1–6.
- [30] S. Lee and H. Shim, "Skewed stereo time-of-flight camera for translucent object imaging," *Image Vision Comput.*, vol. 43, no. C, pp. 27–38, 2015.

- [31] N. Naik, A. Kadambi, C. Rhemann, S. Izadi, R. Raskar, and S. BingKang, "A light transport model for mitigating multipath interference in time-of-flight sensors," in *Proc. IEEE Conf. Comput. Vis. Pattern Recognit.*, 2015, pp. 73–81.
- [32] A. Kadambi, J. Schiel, and R. Raskar, "Macroscopic interferometry: Rethinking depth estimation with frequency-domain time-of-flight," in *Proc. IEEE Conf. Comput. Vis. Pattern Recognit.*, 2016, pp. 893–902.
- [33] N. Naik, S. Zhao, A. Velten, R. Raskar, and K. Bala, "Single view reflectance capture using multiplexed scattering and time-of-flight imaging," *ACM Trans. Graphics*, vol. 30, no. 6, pp. 171:1–171:10, 2011.
- [34] F. Heide, L. Xiao, W. Heidrich, and M. B. Hullin, "Diffuse mirrors: 3D reconstruction from diffuse indirect illumination using inexpensive time-of-flight sensors," in *Proc. IEEE Conf. Comput. Vis. Pattern Recognit.*, 2014, pp. 3222–3229.
- [35] A. Kadambi, H. Zhao, B. Shi, and R. Raskar, "Occluded imaging with time-of-flight sensors," *ACM Trans. Graphics*, vol. 35, no. 2, pp. 15:1–15:12, 2016.
- [36] C.-Y. Tsai, K. N. Kutulakos, S. G. Narasimhan, and A. C. Sankaranarayanan, "The geometry of first-returning photons for non-line-of-sight imaging," in *Proc. IEEE Conf. Comput. Vis. Pattern Recognit.*, 2017, pp. 2336–2344.
- [37] H. Shim and S. Lee, "Recovering translucent object using a single time-of-flight depth camera," *IEEE Trans. Circuits Syst. Video Technol.*, vol. 26, no. 5, pp. 841–854, May 2016.
- [38] K. Tanaka, Y. Mukaigawa, H. Kubo, Y. Matsushita, and Y. Yagi, "Recovering transparent shape from time-of-flight distortion," in *Proc. IEEE Conf. Comput. Vis. Pattern Recognit.*, 2016, pp. 4387–4395.
- [39] M. O'Toole, F. Heide, L. Xiao, M. B. Hullin, W. Heidrich, and K. N. Kutulakos, "Temporal frequency probing for 5D transient analysis of global light transport," *ACM Trans. Graphics*, vol. 33, no. 4, pp. 87:1–87:11, 2014.
- [40] M. Gupta, S. K. Nayar, M. B. Hullin, and J. Martin, "Phasor imaging: A generalization of correlation-based time-of-flight imaging," *ACM Trans. Graphics*, vol. 34, no. 5, pp. 156:1–156:18, 2015.
- [41] A. C. Thompson, S. A. Wade, P. J. Cadusch, W. G. Brown, and P. R. Stoddart, "Modeling of the temporal effects of heating during infrared neural stimulation," *J. Biomed. Opt.*, vol. 18, no. 3, 2013, Art. no. 035004.
- [42] Y. Ito, R. P. Kennan, E. Watanabe, and H. Koizumi, "Assessment of heating effects in skin during continuous wave near-infrared spectroscopy," *J. Biomed. Opt.*, vol. 5, no. 4, pp. 383–391, 2000.
- [43] P. Saponaro, S. Sorensen, A. Kolagunda, and C. Kambhamettu, "Material classification with thermal imagery," in *Proc. IEEE Conf. Comput. Vis. Pattern Recognit.*, 2015, pp. 4649–4656.
- [44] D. Miyazaki, M. Saito, Y. Sato, and K. Ikeuchi, "Determining surface orientations of transparent objects based on polarization degrees in visible and infrared wavelengths," *J. Opt. Soc. America A*, vol. 19, no. 4, pp. 687–694, 2002.
- [45] G. Eren *et al.*, "Scanning from heating: 3D shape estimation of transparent objects from local surface heating," *Opt. Express*, vol. 17, no. 14, pp. 11 457–11 468, 2009.
- [46] R. J. Woodham, "Photometric method for determining surface orientation from multiple images," *Opt. Eng.*, vol. 19, no. 1, pp. 139–144, 1980.
- [47] S. K. Nayar, X.-S. Fang, and T. Boulton, "Separation of reflection components using color and polarization," *Int. J. Comput. Vision*, vol. 21, no. 3, pp. 163–186, 1997.
- [48] T. Treibitz, Z. Murez, B. G. Mitchell, and D. Kriegman, "Shape from fluorescence," in *Proc. Eur. Conf. Comput. Vis.*, 2012, pp. 292–306.
- [49] C. Inoshita, Y. Mukaigawa, Y. Matsushita, and Y. Yagi, "Surface normal decomposition: Photometric stereo for optically thick translucent objects," in *Proc. Eur. Conf. Comput. Vis.*, 2014, pp. 346–359.
- [50] T. T. Ngo, H. Nagahara, and R. Taniguchi, "Shape and light directions from shading and polarization," in *Proc. IEEE Conf. Comput. Vis. Pattern Recognit.*, 2015, pp. 2310–2318.
- [51] Z. Murez, T. Treibitz, R. Ramamoorthi, and D. J. Kriegman, "Photometric stereo in a scattering medium," *IEEE Trans. Pattern Anal. Mach. Intell.*, vol. 39, no. 9, pp. 1880–1891, Sep. 2017.
- [52] J. R. Howell, M. P. Mengüç, and R. Siegel, *Thermal Radiation Heat Transfer, Sixth Edition*. Boca Raton, FL, USA: CRC Press, 2015.
- [53] B. Sun, K. Sunkavalli, R. Ramamoorthi, P. N. Belhumeur, and S. K. Nayar, "Time-varying BRDFs," *IEEE Trans. Vis. Comput. Graphics*, vol. 13, no. 3, pp. 595–609, May 2007.
- [54] H. W. Jensen, S. R. Marschner, M. Levoy, and P. Hanrahan, "A practical model for subsurface light transport," in *Proc. 28th Annu. Conf. Comput. Graphics Interactive Technol.*, 2001, pp. 511–518.
- [55] P. Hanrahan and W. Krueger, "Reflection from layered surfaces due to subsurface scattering," in *Proc. 20th Annu. Conf. Comput. Graphics Interactive Technol.*, 1993, pp. 165–174.
- [56] K. Tanaka, Y. Mukaigawa, H. Kubo, Y. Matsushita, and Y. Yagi, "Recovering inner slices of layered translucent objects by multi-frequency illumination," *IEEE Trans. Pattern Anal. Mach. Intell.*, vol. 39, no. 4, pp. 746–757, Apr. 2017.
- [57] J. Unsworth and F. Duarte, "Heat diffusion in a solid sphere and fourier theory: An elementary practical example," *Amer. J. Phys.*, vol. 47, no. 11, pp. 981–983, 1979.
- [58] H. S. Carslaw and J. C. Jaeger, *Conduction of Heat in Solids*, 2nd ed. Oxford, U.K.: Clarendon Press, 1959.
- [59] J. Crank and P. Nicolson, "A practical method for numerical evaluation of solutions of partial differential equations of the heat-conduction type," *Math. Proc. Cambridge Philos. Soc.*, vol. 43, no. 1, pp. 50–67, 1947.
- [60] T. W. Becker and B. J. P. Kaus, "Numerical modeling of earth systems—An introduction to computational methods with focus on solid earth applications of continuum mechanics," Lecture notes for USC GEOL557, v. 1.1.4, 2016. [Online]. Available: <http://www-udc.ig.utexas.edu/external/becker/preprints/Geodynamics557.pdf>
- [61] T. Maeda, Y. Wang, R. Raskar, and A. Kadambi, "Thermal non-line-of-sight imaging," in *Proc. IEEE Int. Conf. Comput. Photography*, 2019, pp. 1–11.



**Kenichiro Tanaka** received the MS and PhD degrees in CS from Osaka University, in 2014 and 2017, respectively. He is currently an assistant professor at the Nara Institute of Science and Technology (NAIST), Japan, and a visiting scholar at UCLA. His research interests include physically-based computer vision and computational photography, imaging, and illumination. He is a member of the IEEE.



**Nobuhiro Ikeya** received the MS degree from the Nara Institute of Science and Technology (NAIST), Japan, in 2018.



**Tsuyoshi Takatani** received the MS and PhD degrees from Osaka University, in 2013, and NAIST, in 2019. He is currently a researcher by special appointment at the National Institute of Informatics (NII), Japan. He was a research engineer at Toshiba Research & Development Center from 2013 to 2016. His research interests include computational optical sensing, imaging, and fabrication. He is a member of IEEE and OSA.



**Hiroyuki Kubo** received the MS and PhD degrees from Waseda University, in 2008 and 2012, respectively. He is currently an assistant professor at the Nara Institute of Science and Technology (NAIST), Japan since 2014. His research interests include computer graphics and computer animation. He is a member of the ACM.



**Takuya Funatomi** received the BS degree in engineering, the MS and PhD degrees in informatics from the Graduate School of Informatics, Kyoto University, Japan, in 2002, 2004, and 2007, respectively. He is currently an associate professor at the Nara Institute of Science and Technology (NAIST), Japan since 2015. He was an assistant professor with Kyoto University, Japan from 2007 to 2015, and a visiting assistant professor at Stanford University, in 2014. His research interests include computer vision, computer graphics, and pattern recognition. He is a member of the IEEE.



**Achuta Kadambi** received the doctorate degree from MIT and joined UCLA as the founding director of the Visual Machines Group. His research group gives robots the gift of sight by blending camera and algorithm design. With applications to cyber-physical systems and digital health, His research has been recognized with best paper awards, Draper Fellowship, Lemelson-MIT Student Prize, and more than 15 US patent filings. In addition to leading the Visual Machines Group, He is currently an assistant professor of Electrical Engineering at UCLA. He is a member of the IEEE.



**Vijay Ravi** is currently working toward the master's degree in the Electrical and Computer Engineering Department, University of California, Los Angeles. He is a member of the IEEE.



**Yasuhiro Mukaigawa** received the ME and PhD degrees from the University of Tsukuba, in 1994 and 1997, respectively. He became a research associate at Okayama University, in 1997, an assistant professor at the University of Tsukuba, in 2003, an associate professor at Osaka University, in 2004, and a professor at the Nara Institute of Science and Technology (NAIST), in 2014. His current research interests include photometric analysis and computational photography. He is a member of the IEEE.

▷ For more information on this or any other computing topic, please visit our Digital Library at [www.computer.org/csdl](http://www.computer.org/csdl).